

# Free surface shapes in rigid body rotation: Exact solutions, asymptotics and approximants.

Enrique Ramé

## Abstract

We analyze steady interface shapes in zero gravity in rotating right circular cylindrical containers under rigid body rotation. Predictions are made near criticality, in which the interface, or part thereof, becomes straight and parallel to the axis of rotation. We examine geometries where the container is axially infinite and derive properties of their solutions. We then examine in detail two special cases of menisci in a cylindrical container: a meniscus spanning the cross section; and a meniscus forming a bubble. In each case we develop exact solutions for the meniscus height and the bubble length as infinite series in powers of appropriate rotation parameters; and we find the respective asymptotic behaviors as the shapes approach their critical configuration. Finally we apply the method of asymptotic approximants to yield analytical expressions for the height of the meniscus and the length of a spinning bubble over the whole range of rotation speeds. As the spinning bubble method is commonly used to measure surface tension, the latter result has practical relevance.

# 1 Introduction

The shapes of fluid interfaces in rigid body rotation have been well studied, with the spinning bubble tensiometer being a notable example, see [1, 2]. Since about the mid 1950s, interest in such problems has grown with the need to engineer fluid containers in zero gravity for spacecraft, where guaranteeing a known location for the liquid phase is crucial for rockets to fire properly. Seebold [3] performed a stability analysis of menisci in circular cylindrical containers in rigid-body rotation with arbitrary axial gravity and contact angle. He derived stability limits by a variational analysis of the Hamilton principle. Later Preziosi & Joseph [4] analyzed the stability of periodic interface shapes in rigid body rotation by minimization of a suitable energy potential under conditions of negligible gravity, obtaining results that are wholly consistent with those of Seebold [3].

Similar to a static meniscus in a gravitational field, the shape of the interface between two immiscible fluids in rigid body rotation with angular velocity  $\omega$ , density difference  $\Delta\rho \equiv \rho_1 - \rho_2$  ( $> 0$ ) and surface tension  $\sigma$ , depends on the rotational Bond number  $\lambda \equiv \Delta\rho\omega^2d^3/\sigma$ , where  $d$  is some appropriate length that depends on the geometry being considered. The studies cited above show that a critical value  $\lambda_c$  exists such that, when  $\lambda \rightarrow \lambda_c$  from below, the interface undergoes a critical transition, with an outcome that depends on the configuration of the fluid body and the particular container. Figure 1 illustrates some typical configurations.

More specifically, Seebold [3] showed that menisci having finite axial length and spanning the entire cross section of a cylinder with contact angle  $\alpha$  at the cylinder wall (such as shown in fig. 1a), exist in zero gravity under rigid body rotation for  $\lambda < 4f(\alpha)$ , where  $f(\alpha)$  is some function of the contact angle and  $f(0) = 1$ . When  $\lambda$  approaches  $4f(\alpha)$  the meniscus reorganizes with a divergent axial length into the shape of a straight cylinder (fig. 1b). Preziosi & Joseph [4] showed that non-straight periodic interfaces that develop in rigid body motions for  $\lambda < 4$  become straight cylinders when when  $\lambda \geq 4$ . This result is entirely consistent with the analysis of Seebold [3], who collected extensive experimental evidence (and also intuited without proof) that shapes become straight cylinders when  $\lambda \geq \lambda_c$ . Ross [5] studied the shapes of rotating drops and bubbles (as shown in fig. 1a for  $\alpha = 0$  and fig. 1c), and obtained several important results and interpretations that coincide with those of Seebold [3] and Preziosi & Joseph [4] in the case of bubbles, and with those of Chandrasekhar [6] in the case of drops.

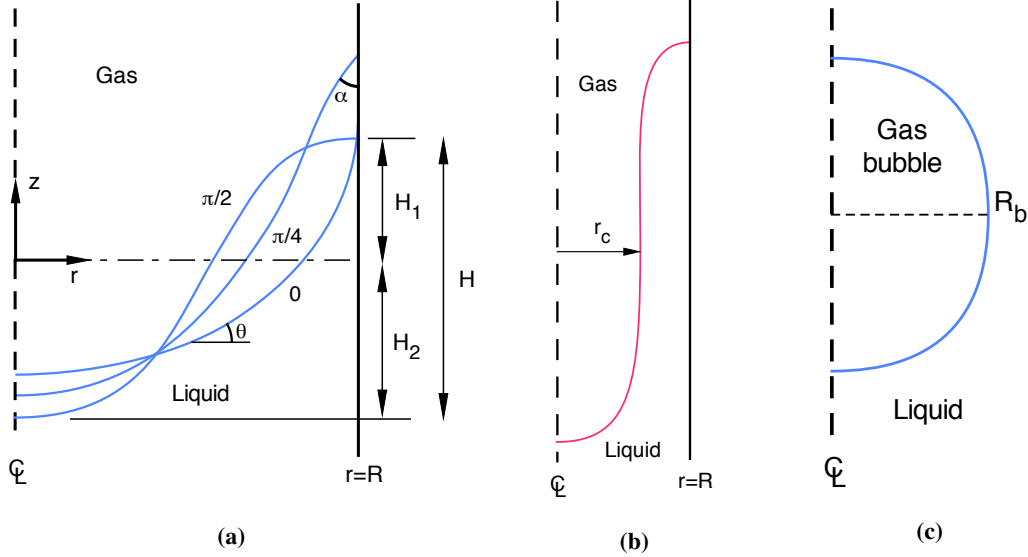


**Figure 1:** Schematics of surface configurations with fluids in rigid body rotation about the axis of a cylindrical container. Liquid is below the interface. (a): typical shapes at  $\lambda < \lambda_c$ , for wall contact angles,  $\alpha = 0, \pi/4$  and  $\pi/2$ , as marked.  $\theta$  is the slope angle of the interface.  $z = 0$  is chosen so that the volumes of liquid above and below are equal.  $H$  is the meniscus length. (b): Shape with  $\lambda$  very close to  $\lambda_c$ , for 90-degree contact angle. Most of the surface is a straight circular cylinder of radius  $r_c$ . The vortex height diverges as  $\lambda \rightarrow \lambda_c$ . (c): Spinning bubble.  $R_b$  is the maximum radius. The half-bubble on either side of the equator is mathematically identical to the zero-contact angle case in fig. 1a.

In this work we derive new results about properties of menisci in rigid body rotation. Specifically, our goal is to develop analytical tools to describe the axial length of menisci in configurations of practical relevance. We analyze two configurations, depicted schematically in fig. 1: 1) a meniscus spanning the cylinder cross section, as in figs. 1a and 1b; and 2) a meniscus forming a bubble whose axis coincides with the axis of rotation, as in fig. 1c. The latter is the same geometry of the spinning bubble tensiometer [1]. For each geometry, we examine the respective shapes and axial lengths as a function of  $\lambda$ . In particular, we identify the asymptotic behaviors of the divergence in axial length (denoted  $H$  in fig. 1) as  $\lambda \rightarrow \lambda_c$  and find that the divergence law depends on the meniscus configuration. We then develop exact solutions for these lengths as infinite series in powers of  $\lambda$ . Since the infinite series solutions converge very poorly near  $\lambda_c$ , we apply the method of asymptotic approximants [7] to describe axial length uniformly over the whole range  $0 \leq \lambda < \lambda_c$  for both configurations.

## 2 Analysis

### 2.1 Formulation

Consider a liquid of density  $\rho$  in contact with a gas of negligible density in a cylindrical container of radius  $R$ , rotating with angular velocity  $\omega$  about its axis in rigid body rotation. The gas-liquid interface has surface tension  $\sigma$ , its location is  $z = h(r)$ , and obeys the normal component of the dynamic boundary condition with a pressure whose gradient arises from the centrifugal acceleration only.

Neglecting the dynamics of the gas and using  $d$  as a characteristic length scale, the dimensionless governing equation is given as

$$\frac{1}{r} \frac{d}{dr} \left( \frac{rh'}{\sqrt{1+h'^2}} \right) = -P_0 - \lambda \frac{r^2}{2}, \quad (1)$$

$$\lambda \equiv \frac{\rho \omega^2 d^3}{\sigma}, \quad (2)$$

where  $h'(r) = \tan \theta$  is the slope relative to the  $r$ -axis,  $P_0$  is the pressure difference across the interface at  $r = 0$  made dimensionless with  $\sigma/d$  and  $\lambda$  is the rotational Bond number. (If the meniscus contacts an interior surface that prevents it from reaching the center line, then  $P_0$  is the pressure difference at  $r = 0$  of the static extrapolation of the meniscus back to  $r = 0$ .) In general, the characteristic length  $d$  depends on the configuration considered, as sketched in fig. 1. If the interface spans the entire radius of the container, then  $d = R$ ; in the case of a bubble wholly surrounded by the liquid, then  $d$  is the maximum radius of the bubble.

Since  $h'(r) = \tan \theta$ , the left-hand side of eq. (1) may be written as  $d(r \sin \theta)/(r dr)$ . This equation may be integrated once to obtain an expression for  $\sin \theta$  vs  $r$  using two appropriate boundary conditions. One boundary condition accounts for the axial symmetry and is imposed to all the cases studied here:

$$\theta(0) = 0. \quad (3)$$

The other boundary condition is applied at the outer end of the interface. In the case of a meniscus spanning the container, the interface obeys a contact angle condition:

$$\theta(1) = \frac{\pi}{2} - \alpha, \quad (4)$$

where  $\alpha$  is the contact angle, as depicted in fig. 1a. In the case of a bubble wholly surrounded by liquid, the second boundary condition is:

$$\theta(1) = \frac{\pi}{2}. \quad (5)$$

Physically, this condition reflects the equatorial symmetry of the bubble; but mathematically it can be seen to be identical to the case of a meniscus with contact angle  $\alpha = 0$  expressed in eq. (4). The shape for arbitrary contact angle  $\alpha$  is therefore:

$$\frac{h'}{\sqrt{1+h'^2}} = \sin \theta = r \cos \alpha + \frac{\lambda}{8} r(1-r^2). \quad (6)$$

where, from the preceding discussion,  $\alpha$  must be set to zero to describe a bubble. A volume condition, specific to each configuration determines  $h(r)$  after one additional integration.

## 2.2 Properties

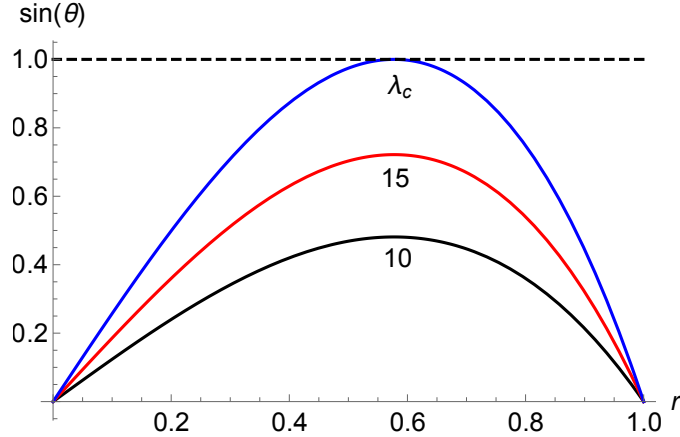


**Figure 2:** Sine of the slope angle, vs.  $r$  at various  $\lambda$  for  $\alpha = \pi/2$ , i.e.,  $\theta(1) = 0$ . When  $\lambda < \lambda_c$ , the maximum slope corresponds to an inflection point with slope  $0 < \theta < \pi/2$ .

Having shown that eq. (6) may be used both for a meniscus spanning the container with arbitrary contact angle  $\alpha$  and for a wholly immersed bubble by setting  $\alpha = 0$ , in this section we examine the case of  $\alpha = \pi/2$ , i.e., normal contact at the container wall. No generality is lost by focusing on this special case; on the contrary, we will show below that, far from being special, critical shapes for arbitrary  $\alpha$  may be obtained from the shape at any other  $\alpha$  by suitable scaling manipulations. Fig. 2 shows  $\sin \theta$  vs  $r$  for various  $\lambda$ . When  $\lambda < \lambda_c$ , the slope attains a local maximum smaller than  $\pi/2$ , hence the maximum slope coincides with an inflection point. However, at  $\lambda_c$  the local maximum

is  $\theta_{\max} = \pi/2$ , and the axial length of the meniscus diverges with infinite slope and with a straight cylindrical shape of radius equal to the location where  $\theta_{\max} = \pi/2$  –in agreement with previous studies, [3, 4]. To find this location, we solve (with  $\alpha$  arbitrary)

$$\sin \theta = 1, \quad \frac{d \sin \theta}{dr} = 0, \quad (7)$$

to find

$$\lambda_c = \frac{4}{r_c^3}, \quad r_c = \frac{1}{2 \cos \left( \frac{1}{3}(\pi - \alpha) \right)}. \quad (8)$$

For  $\alpha = \pi/2$ ,  $\lambda_c = 12\sqrt{3}$  and  $r_c = 1/\sqrt{3}$ . Eqs. (8) provide exact relations in support of the numerical results of Seibold [3] for zero gravity. In particular, if one views the vertical slope location,  $r_c$ , as the radius of a straight circular cylinder, the rotational Bond number can be written as  $\bar{\lambda}_c \equiv r_c^3 \lambda_c = 4$ ; this result agrees with previous work [3, 4].

An important property of critical shapes is that  $\alpha = \pi/2$  generates a master shape from which all other critical shapes with  $0 \leq \alpha \leq \pi$  may be constructed. The method is as follows: Starting with the critical shape for  $\alpha = \pi/2$ , and denoting the independent variable as  $r^*$ , we set  $\lambda = \lambda_c^* = 12\sqrt{3}$  and, using eq. (6), determine  $r_w^*$  such that the slope is  $\pi/2 - \alpha$ , i.e.,  $r_w^*$  is the location where the critical master shape has the same slope as the wall contact slope of interest:  $\cos \alpha = (\lambda_c^*/8)(r_w^* - r_w^{*3})$ , i.e.,  $r_w^*$  is the location where the critical master shape has the same slope as the wall contact slope of interest:

$$r_w^* = \frac{2}{\sqrt{3}} \cos \left( \frac{1}{3}(\pi - \alpha) \right). \quad (9)$$

We then rescale  $r^*$ ,

$$r = \frac{r^*}{r_w^*}. \quad (10)$$

Substituting for  $r^*$  and manipulating to expose the binomial  $(r - r^3)$ , we obtain the critical shape with  $\theta(1) = \pi/2 - \alpha$ :

$$\sin \theta = r \cos \alpha + \frac{\lambda_c}{8}(r - r^3), \quad (11)$$

where  $\lambda_c$  satisfies eqs. (8). This is the same equation that is solved in eq. (6) with arbitrary  $\alpha$  for  $\lambda = \lambda_c$ .

## 2.3 Meniscus spanning the container radius

When the meniscus spans the cylinder radius  $R$ , we identify  $d = R$ . One integration of eq. (6) with a volume condition fixes the absolute height of the interface. In a reference frame where the liquid volumes above and below  $z = 0$  are equal:

$$\int_0^1 h r dr = 0. \quad (12)$$

The integration to compute  $h(r)$  must be performed numerically. We focus on the case of normal contact ( $\alpha = \pi/2$ ). This case is special only because the maximum slope location is  $r_c = 1/\sqrt{3}$  for all  $\lambda$ . Apart from this distinction, interface shapes are qualitatively similar when contact is not normal; and, as stated in sec. 2.2, interface shapes at criticality are easily scaled across different contact angles.

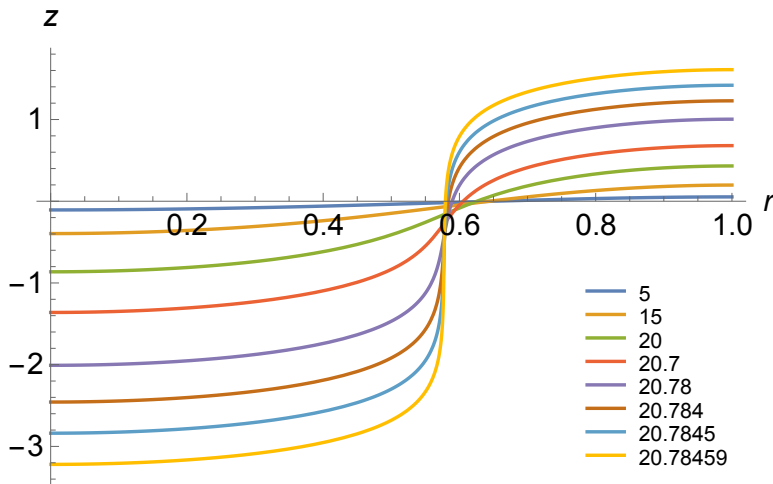


**Figure 3:** Shapes with normal contact at  $r = 1$  (contact angle  $\alpha = \pi/2$ ) for values of  $\lambda$  noted in legend.

The shape nearest  $z = 0$  is for  $\lambda = 5$ . Consecutive values of  $\lambda$  apply to shapes further away from  $z = 0$ , showing the divergence of the depth as  $\lambda \rightarrow \lambda_c = 12\sqrt{3} \approx 20.78459\dots$

### 2.3.1 Meniscus asymptotics for $\lambda \approx 12\sqrt{3}$

Fig. 3 shows interface shapes  $z = h(r)$  when  $\alpha = \pi/2$ , obtained numerically by integrating  $h'$  given by eq. (6). It is clear that the axial length of the meniscus,  $H = \int_0^1 h' dr$ , diverges as  $\lambda \rightarrow \lambda_c$ . Identifying the leading asymptotic behavior of this divergence is of considerable theoretical and practical interest because it helps control devices such as rotating reactors where two immiscible fluids of differing densities are present. Since  $h'(r_c) \rightarrow \infty$  as  $\lambda \rightarrow \lambda_c$ , it follows that  $h'$  develops

a narrowing peak around the maximum slope location,  $r_c$ ; and that the area under the peak –though divergent– depends to leading order on the shape of this peak only, i.e., it is independent of the details outside the peak. To begin, we identify the radial scale around the peak. Let

$$\epsilon \equiv \lambda_c - \lambda, \quad \eta \equiv \frac{r - r_c}{\epsilon^p}, \quad (13)$$

where  $\epsilon \ll 1$ ,  $\eta$  is a stretched radial distance centered at the peak, and  $p$  needs to be determined.

Approximating  $h' \sim \frac{1}{\sqrt{1-\sin^2 \theta}}$  near  $r_c$ , and substituting  $r$  and  $\lambda$  from eq. (13), we find that

$$1 - \sin^2 \theta \sim \epsilon \frac{\sqrt{3}}{18} + \epsilon^{2p} 9 \eta^2, \quad \epsilon \rightarrow 0. \quad (14)$$

This suggests that, for  $h'$  to be integrable at  $\eta = 0$  we must have  $p = 1/2$  so that

$$h' \sim h'_{\text{asy}} = \frac{1}{3 \sqrt{\epsilon} \sqrt{\frac{1}{54\sqrt{3}} + \eta^2}}. \quad (15)$$

Thus, the leading behavior of  $H$  may be found in closed form from

$$H \sim \int_{-\frac{1}{\sqrt{3\epsilon}}}^{(1-\frac{1}{\sqrt{3}})\frac{1}{\sqrt{\epsilon}}} \frac{d\eta}{3 \sqrt{\frac{1}{54\sqrt{3}} + \eta^2}}, \quad (16)$$

and then expanding for  $\epsilon \rightarrow 0$ :

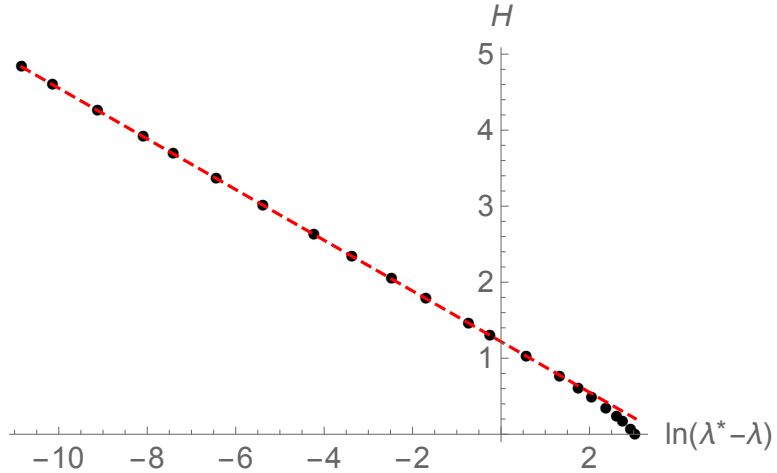


**Figure 4:** Comparison of numerical and asymptotic evaluations of depth  $H$ .  $\lambda_c - \lambda = \epsilon$  and  $\lambda_c = 12\sqrt{3}$ .  
Black dots: numerical. Dashed line: eq. (17).

$$H \sim H_{\text{asy}} = -\frac{1}{3} \ln \epsilon + H_0. \quad (17)$$

$H_0$  is an  $O(1)$  constant and is found by numerical integration,

$$H_0 = \lim_{\epsilon \rightarrow 0} \int_0^1 (h' - h'_{\text{asy}}) dr \approx 1.218, \quad (18)$$

Fig. 4 shows the agreement between the numerical and asymptotic evaluations of the meniscus depth.

### 2.3.2 Series solution for $H(\lambda)$

In order to have a description of  $H(\lambda)$  over the rest of the  $\lambda$ -domain, we now seek a series solution for  $H(\lambda)$  in powers of  $\lambda$  about  $\lambda = 0$ . Since  $\sin \theta \sim \lambda$  for  $\alpha = \pi/2$ , it follows that  $h'(r, \lambda)$ , obtained from eq. (6),

$$h'(r, \lambda) = \frac{\sin \theta}{\sqrt{1 - \sin^2 \theta}}, \quad (19)$$

may be expanded in a Taylor series about  $\lambda = 0$  as

$$h'(r, \lambda) = \sum_{n=0}^{\infty} a_{2n+1} (\sin \theta)^{2n+1} = \sum_{n=0}^{\infty} a_{2n+1} \left( \frac{r - r^3}{8} \right)^{2n+1} \lambda^{2n+1}, \quad (20)$$

where

$$a_1 = 1, \quad a_n = a_{n-2} \left( \frac{n-2}{n-1} \right), \quad n = 3, 5, 7, 9, \dots \quad (21)$$

As seen in fig. 2,  $\sin \theta$  remains below 1 for  $\lambda < \lambda_c$ . Thus, the series in eq. (20) converges for  $\lambda < \lambda_c$  and may be integrated term by term to obtain the meniscus length:

$$H(\lambda) = \sum_{n=0}^{\infty} a_{2n+1} b_{2n+1} \lambda^{2n+1}, \quad (22)$$

where

$$b_n = \frac{1}{8^n} \int_0^1 (r - r^3)^n dr, \quad n \text{ odd.} \quad (23)$$

It is easy to show that  $b_1 = 1/32$  and

$$b_{n+2} = \frac{1}{64} \frac{(n+2)(n+1)}{\left(\frac{3n+7}{2}\right) \left(\frac{3n+5}{2}\right) \left(\frac{3n+3}{2}\right)} b_n. \quad (24)$$

Even though this series solution was motivated by a desire to examine the small- $\lambda$  behavior of  $H$ , the ability to compute all the terms of the infinite series permits evaluation of the radius of convergence of the series given in eq. (22). The ratio criterion guarantees convergence iff

$$\lim_{n \rightarrow \infty} \frac{a_{2n+1}}{a_{2n-1}} \frac{b_{2n+1}}{b_{2n-1}} \lambda^2 < 1. \quad (25)$$

Evaluation of this criterion using eqs. (21) and (24) shows that the series does converge for  $\lambda < 12\sqrt{3} = \lambda_c$  as was stated above. Thus, eq. (22) is an exact solution. Unfortunately, though, the convergence is poor and nonuniform with increasing  $\lambda$  beyond  $\lambda \approx 15$  due to the influence of the logarithmic singularity, see sec. 2.3.1. In sec. 2.5 we use asymptotic approximants to generate a rapidly converging and uniform representation of  $H(\lambda)$  over the entire range  $0 \leq \lambda < 12\sqrt{3}$ .

## 2.4 Spinning bubble

If the gas volume in a finite container is small enough, or the axial dimension of the container is long enough, the bubble can become critical (i.e., it can adopt a straight circular cylindrical shape) before the interface touches the end plates of the container. This is the basis for the well-known spinning bubble method to determine surface tension [1, 2]. In this geometry (see fig. 1c) and in zero-gravity,  $\lambda < \lambda_c = 4$ , and the characteristic length,  $d$ , is the maximum bubble radius,  $R_b$ . For extensive detail on the challenges of interpreting and operating the spinning drop tensiometer in a gravitational field, see Manning & Scriven [8] and references therein.

In this section we derive the asymptotic behavior of the bubble shape as  $\lambda \rightarrow 4$ , which can be used to better inform the bubble length being measured; and develop a solution for the bubble length as a series in powers of  $\lambda$ . Using the bubble maximum radius,  $R_b$ , as the characteristic length, the slope angle of the interface relative to the  $r$ -axis is found by integrating eq. (6) subject to  $\theta(0) = 0$ ,  $\theta(1) = \pi/2$ :

$$\sin \theta = r + \frac{\lambda}{8}r(1 - r^2). \quad (26)$$

Since  $\sin \theta = h'/\sqrt{1 + h'^2}$ , numerical integration with a volume condition yields the interface shape,  $z = h(r)$ . The bubble has infinite slope ( $\theta_{\max} = \pi/2$ ) for all  $\lambda$  at  $r = 1$ , in contrast with the vortex analyzed in sec. 2.3 where the maximum slope is at an inflection point with  $\theta_{\max} < \pi/2$  and  $0 < r < 1$ , and  $\theta_{\max} \rightarrow \pi/2$  only as  $\lambda \rightarrow \lambda_c$ . To probe the character of the spinning bubble shape, we note that, when  $\lambda < 4$ ,  $dr/dz = 0$  at  $(r, z) = (1, 0)$  but  $d^2r/dz^2 < 0$  there. This suggests that  $1 - r \sim z^2$ , so that  $\sin \theta \sim 1 - A(1 - r)$  as  $r \rightarrow 1$  for some constant  $A$ . In contrast, when the shape is critical at  $\lambda = 4$ , the end-cap shape approaches a straight cylinder asymptotically at a distance from the bubble tip that is large compared with the radius; therefore, in the critical condition,  $1 - r \sim \exp[B(H - z)]$  for some constant  $B$ , where  $(r, z) = (0, H)$  is the tip location. This implies that  $\sin \theta \sim 1 - C(1 - r)^2$  as  $r \rightarrow 1$  for  $\lambda = 4$  and some constant  $C$ . We conclude,

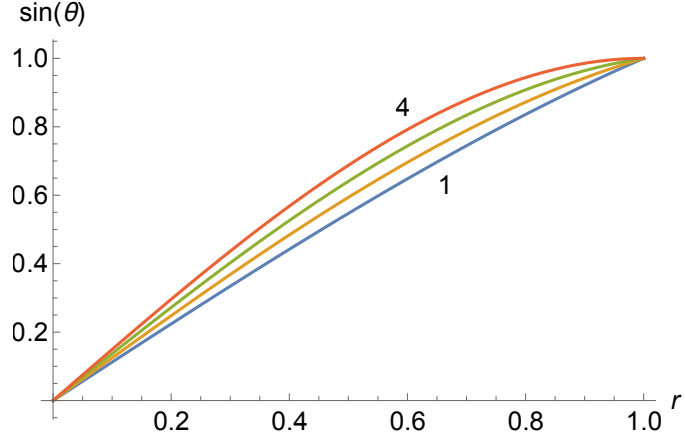


**Figure 5:** Shapes of spinning bubbles at various  $\lambda = 1, 2, 3, 4$ . Only  $\lambda = 4$  has zero slope  $d(\sin \theta)/dr$  at  $r = 1$ .

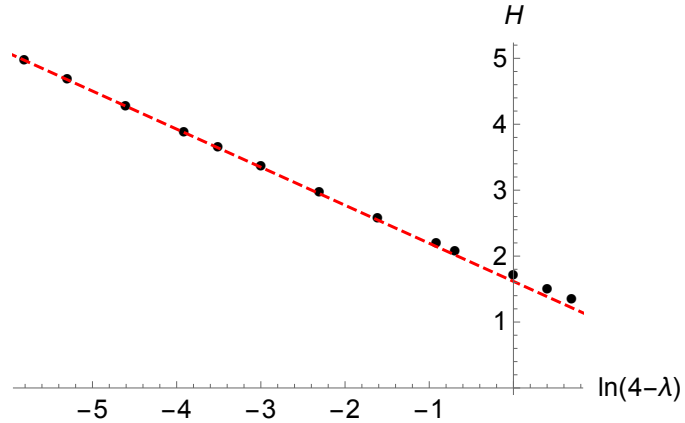


**Figure 6:** Length of spinning bubble vs.  $\lambda$ . Dots: numerical, eq. (26). Dashed line: Asymptotics, eq. (31).

therefore, that the critical shape requires

$$\frac{d(\sin \theta)}{dr} = 0 \quad \text{at } r = 1, \lambda = 4 \quad (27)$$

whereas subcritical shapes satisfy

$$\frac{d(\sin \theta)}{dr} > 0 \quad \text{at } r = 1, \lambda < 4. \quad (28)$$

Not surprisingly, the shapes of eq. (26), a few of which are shown in fig. 5, display these properties. In contrast to the meniscus spanning the cylinder radius, the distinct character of the spinning bubble configuration is that  $\sin \theta = 1$  always at  $r = 1$ ; but  $d(\sin \theta)/dr \neq 0$  at  $r = 1$  unless  $\lambda = \lambda_c = 4$ .

### 2.4.1 Asymptotics for $\lambda \approx 4$

We derive the asymptotic behavior of the shape as  $\lambda \rightarrow 4$  by the same method of sec. 2.3.1. Let  $\epsilon \equiv 4 - \lambda$  and  $\eta \equiv (r - 1)/\epsilon^p$ , where  $p > 0$  is to be determined. It may be shown that, when  $\epsilon$  is small,

$$\sin^2 \theta \sim 1 - 3\epsilon^{2p}\eta^2 + \epsilon^{1+p}\frac{\eta}{2} + \dots \quad (29)$$

The only choice that ensures integrability at  $\eta = 0$  is  $p = 1$ , yielding

$$h' \sim h'_{asy} = \frac{1}{\epsilon} \frac{1}{\sqrt{3\eta^2 - \frac{\eta}{2}}}. \quad (30)$$

The half-length of the near-critical bubble is then

$$H_{asy} = \int_{-\frac{1}{\epsilon}}^0 \frac{1}{\sqrt{3\eta^2 - \frac{\eta}{2}}} d\eta \sim -\frac{1}{\sqrt{3}} \ln(4 - \lambda) + H_0, \quad \lambda \rightarrow 4. \quad (31)$$

where the constant  $H_0 \approx 1.6166$  is found using the method of eq. (18). Fig. 6 shows a comparison of the numerical and the asymptotic interface shapes.

The (dimensionless) volume depends on  $\lambda$ :

$$V(\lambda) = 2\pi \int_0^1 h(r, \lambda) r dr \quad (32)$$

and provides a relation between the dimensional volume and maximum radius. The closer the bubble is to the critical configuration the closer its shape is to a straight cylinder of radius 1, hence the volume grows progressively more linearly with  $\pi H$  as  $\lambda \rightarrow 4$ . A fit of the numerical volume evaluation shows that

$$V \sim \pi H - 2.09, \quad H \gg 1, \quad (33)$$

in good agreement with the asymptotic behavior of Ross' exact expression for the volume (eqn. 15 in ref. [5]) as  $\lambda \rightarrow 4$ .

### 2.4.2 Series solution for $H(\lambda)$

In order to construct a Taylor series representation of the bubble half-length, we note that, as in Sec. 2.3,  $h' = \sin \theta / \sqrt{1 - \sin^2 \theta}$ . However, in contrast to that analysis, here  $\sin \theta \neq O(\lambda)$ , which

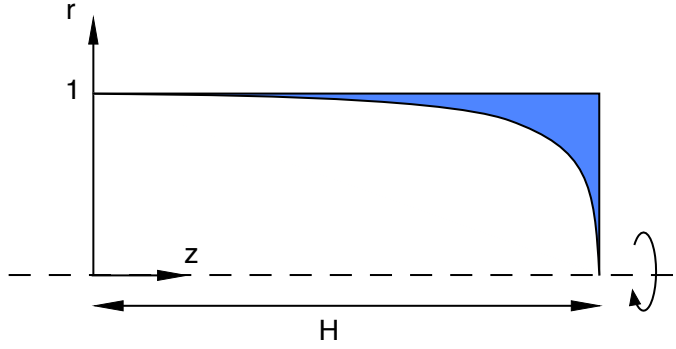


**Figure 7:** Schematic of a half-bubble spinning about the  $z$ -axis. The blue area represents the liquid and is equal to the volume deficit of the actual bubble relative to a straight circular cylinder where the bubble is inscribed. The spinning container is larger than the bubble size and is not shown.

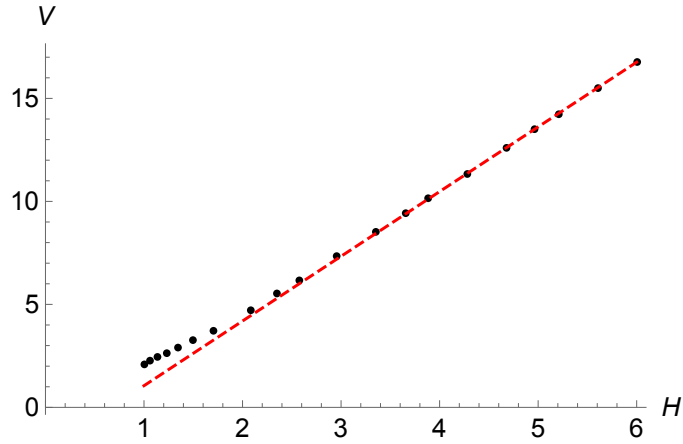


**Figure 8:** Volume vs bubble half-length  $H$ . Dashed line:  $V_{asy} = \pi H - 2.09$ .

complicates evaluation of a Taylor series in powers of  $\lambda$  for  $H(\lambda) = \int_0^1 h' dr$ . One way to obtain this series is to first generate the series

$$h'(r, \lambda) = \sum_{n=0}^{\infty} c_n(r) \lambda^n. \quad (34)$$

Let

$$\sin \theta = A(r) + \lambda B(r) \quad (35)$$

where  $A = r$  and  $B = \frac{r-r^3}{8}$ . Now the denominator in the expression for  $h'$  is

$$\sqrt{1 - A^2 - 2\lambda AB - \lambda^2 B^2} = \left( \sum_{j=0}^2 a_j \lambda^j \right)^{1/2}, \quad (36)$$

where  $a_0 = 1 - A^2$ ,  $a_1 = -2AB$  and  $a_2 = -B^2$ . Using J.C.P. Miller's formula for the series expansion of a series raised to any power [9], we evaluate the series for the inverse of (36):

$$\left( \sum_{j=0}^2 a_j \lambda^j \right)^{-1/2} = \sum_{j=0}^{\infty} b_j \lambda^j, \quad (37)$$

to find the following recursion for the coefficients,

$$\begin{aligned} c_0 &= A b_0 \\ c_{n>0} &= A b_n + B b_{n-1}, \end{aligned} \quad (38)$$

where

$$\begin{aligned} b_0 &= \frac{1}{\sqrt{1 - A^2}}, & b_1 &= \frac{AB}{\sqrt{1 - A^2}}; \\ b_{n>1} &= -\frac{1}{n(1 - A^2)} \left[ \left( \frac{1}{2} - n \right) 2AB b_{n-1} + (1 - n) B^2 b_{n-2} \right]. \end{aligned} \quad (39)$$

Since  $c_n$ 's are linear combinations of  $b_n$ 's, convergence properties of the series in eq. (34) can be determined from those of  $\sum_n b_n \lambda^n$ . Dividing through by  $b_{n-1}$  in eq. (39) we form two ratios of consecutive  $b_n$ . Assuming that this ratio has a limit,  $R_\infty(r)$ , say, as  $n \rightarrow \infty$ , solving a quadratic equation yields  $R_\infty(r) = (r^2 + r)/8$ . Based on the ratio criterion, convergence is guaranteed iff  $\text{Max}_r[R_\infty(r)] \lambda < 1$ , i.e.,  $\lambda < 4$ . As in the problem of sec. 2.3, the series in eq. (34) converges in the entire range of  $\lambda$  where shapes exist, i.e.,  $0 \leq \lambda < 4$ , and is therefore an exact solution. It can therefore be integrated term-by-term to produce another convergent exact solution for  $H(\lambda)$ , e.g.,

$$H(\lambda) = \sum_{n=0}^{\infty} \left( \int_0^1 c_n(r) dr \right) \lambda^n = \sum_{n=0}^{\infty} C_n \lambda^n \quad (40)$$

In the appendix we show an evaluation of  $C_n$  without recursion. Because convergence of series 40 is poor as  $\lambda$  increases beyond  $\lambda \approx 3.5$ , we show in Sec. 2.5 how to implement the method of asymptotic approximants to obtain an analytical expression for  $H(\lambda)$  that is uniform across the entire range  $0 \leq \lambda \leq 4$ .

## 2.5 Approximants

Asymptotic approximants provide uniformly convergent approximations to  $H(\lambda)$  defined in eqs. (22) (the height of a rotating meniscus) and (40) (the length of a spinning bubble) over their entire respective intervals  $0 \leq \lambda \leq \lambda_c$ . The method has most recently been revisited and reexamined by Barlow et al. [7], and interested readers may consult their article and references therein for an

extensive presentation of the method applied to problems covering a broad range of physics.

Briefly, asymptotic approximants go beyond Padé in that they incorporate asymptotic behaviors that are often singular in ways other than just poles [10], thus dramatically improving the approximant's power to extend the region of convergence. Both power series for  $H(\lambda)$  in the present work (eqs. (22) and (40)) have logarithmic divergence at their respective  $\lambda_c$ . Because we have the power series expanded about  $\lambda = 0$ , as well as the logarithmic divergence behavior as  $\lambda$  approaches  $\lambda_c$ , an asymptotic approximant may be used to join these behaviors. In the two problems considered here, we propose the following approximant for  $H(\lambda)$  defined in eqs. (22) and (40):

$$H_A(\lambda, N) = \sum_{n=0}^N A_n(\lambda_c - \lambda)^n + A_L + B_L \log(\lambda_c - \lambda), \quad (41)$$

where  $A_L$  and  $B_L$  have been computed from the respective asymptotic analyses in eqs. (17) and (31). The coefficients  $A_i$  are determined from the condition that the  $N$ -term Taylor series of  $H_A(\lambda, N)$  about  $\lambda = 0$  is equal to the  $N$ -term Taylor series of  $H(\lambda)$  (eqs. (22) and (40)). The form in eq. (41) imposes the fully stripped-off asymptotic logarithmic divergence as  $\lambda \rightarrow \lambda_c$ .

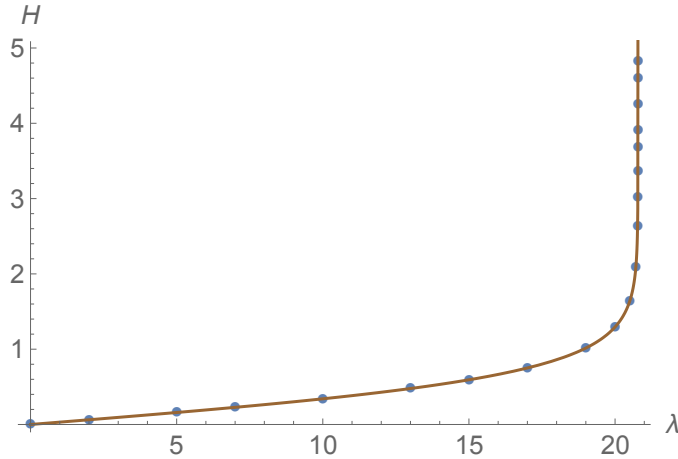


**Figure 9:** The height of the rotating meniscus versus  $\lambda$ . Dots: numerical calculation. Line: 20-term  $H_A$ ;  $A_L = 1.218$ ,  $B_L = 1/3$ . At  $\lambda = 0$  the interface is flat, therefore  $H(0) = 0$ .

The form of an asymptotic approximant to a given function is not uniquely determined but experience allows one to pose forms that exhibit superior convergence. In this work we have not attempted to optimize the form of the approximant that minimizes the number of terms  $N$  required to produce a given error. Figures 9-10 show the numerically calculated  $H(\lambda)$  and  $H_A(\lambda, N)$  for the

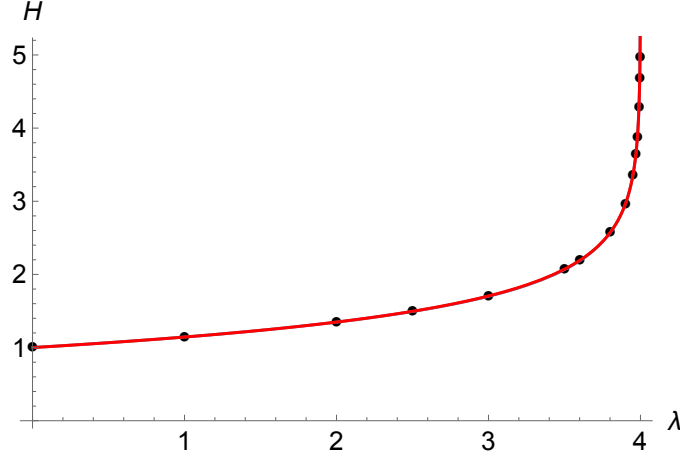


**Figure 10:** The half-length of the spinning bubble versus  $\lambda$ . Dots: numerical calculation. Two solid lines, the 5-term and 10-term  $H_A$ , are indistinguishable;  $A_L = 1.6166$ ,  $B_L = 1/\sqrt{3}$ . At  $\lambda = 0$  and in zero-gravity, the bubble is spherical, i.e.,  $H(0) = 1$ .

rotating meniscus and the spinning bubble, respectively.

We define the error of the  $N$ -term approximant,  $\text{Err}_N(\lambda)$ , as the pointwise absolute error between  $H_A(\lambda, N)$  and the numerical values of  $H$ . Both approximants seem to converge to the numerical calculation as  $N$  increases; but, as shown in figs. 11 and 12, the convergence has a small non-uniformity near  $\lambda_c$ . This is a well-known phenomenon due to remaining singularities that approach zero as  $\lambda \rightarrow \lambda_c$  [11]. The largest errors of the most accurate approximants calculated are  $\text{Err}_{20} \approx 4 \times 10^{-4}$  for the rotating meniscus and  $\text{Err}_{15} \approx 3.6 \times 10^{-3}$  for the spinning bubble.

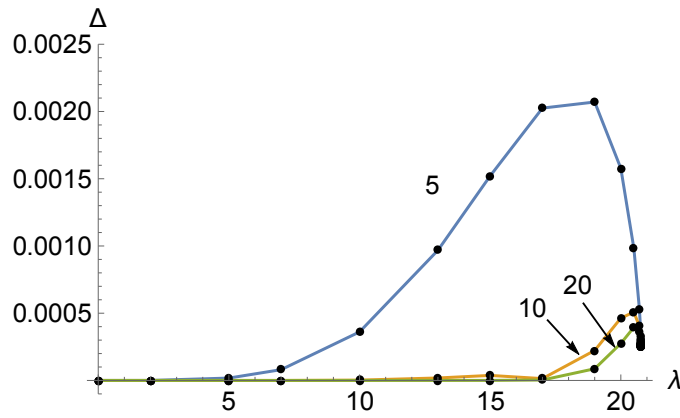


**Figure 11:** Pointwise error,  $|H(\lambda) - H_A(\lambda)|$ , at numerically calculated points for the rotating meniscus for approximants with number of terms  $N$  as indicated.

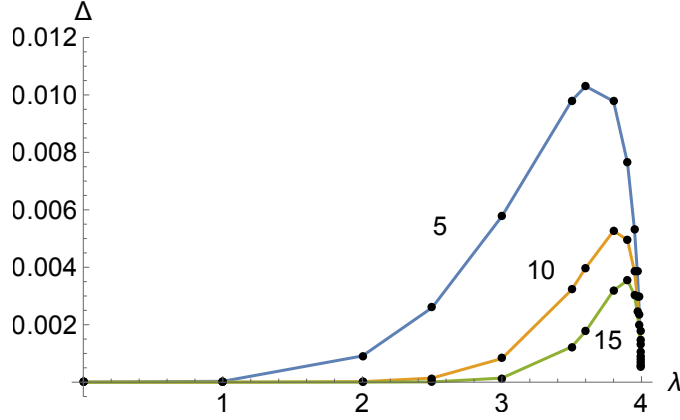


**Figure 12:** Pointwise error,  $|H(\lambda) - H_A(\lambda)|$ , at numerically calculated points for the spinning bubble for approximants with number of terms  $N$  as indicated.

### 3 Discussion

In configurations with arbitrary wall contact angle, the shape is described by eq. (6), rewritten here,

$$\sin \theta = r \cos \alpha + \frac{\lambda}{8}(r - r^3). \quad (42)$$

For a given  $\alpha$  it is instructive to find the smallest  $\lambda$  for which  $\sin \theta$  has a maximum at  $r = 1$ . By requiring that  $d(\sin \theta)/dr = 0$  at  $r = 1$  this value is found to be  $\lambda_{\min} = 4 \cos \alpha$ . In order to achieve criticality in  $0 < r < 1$ ,  $\lambda$  must be greater than  $\lambda_{\min}$ . The location of the maximum slope for  $\lambda > \lambda_{\min}$  is found to be

$$r_0 = \left[ \frac{1}{3} \left( 1 + \frac{8}{\lambda} \cos \alpha \right) \right]^{1/2}. \quad (43)$$

Inserting this result into the expression for  $\sin \theta$  above, we find the maximum value of  $\sin \theta$  for a given  $\alpha$  as function of  $\lambda$ :

$$\sin \theta|_{r_0} = \frac{1}{3\sqrt{3}} \frac{\lambda}{8} \left( 1 + \frac{8}{\lambda} \cos \alpha \right)^{3/2}. \quad (44)$$

This expression becomes 1 when  $\lambda = \lambda_c$  as given in eq. (8). Fig. 13 illustrates this argument for  $\alpha = \pi/3$ . Shapes do exist for  $\lambda < \lambda_{\min}$  but without an inflection point. As  $\lambda$  increases beyond  $\lambda_{\min}$ , the inflection point moves down from  $r = 1$  toward smaller  $r$  and the slope at the inflection becomes increasingly vertical as  $\lambda$  approaches  $\lambda_c$ . Fig. 14 shows the location of the inflection (where  $\sin \theta$  is maximum) versus  $\lambda$ .

The length of the rotating meniscus has two qualitatively different configuration types. The first

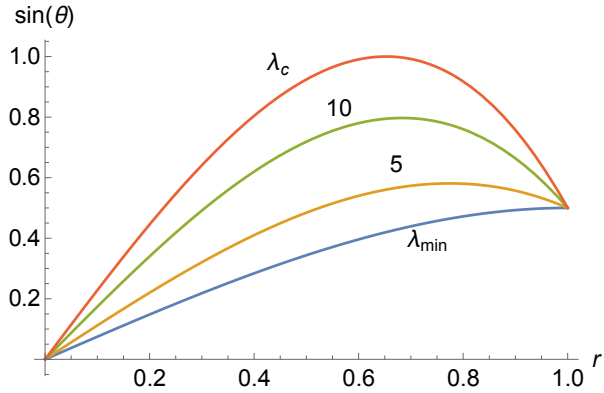


**Figure 13:** Shapes for  $\alpha = \pi/3$  (60-deg contact angle) at various rotation rates.  $\lambda_{\min} = 2$  and  $\lambda_c \approx 14.385$ . The location of the maximum at each  $\lambda$  is plotted below in fig. 14.

type is associated to contact angles larger than zero. In these cases, the radial position of the maximum slope,  $r_0$ , corresponds to an inflection point, e.g.,  $h'(r_0) > 0$ ,  $h''(r_0) = 0$  (i.e., zero curvature) for all  $\lambda < \lambda_c$ . The normal contact case we analyzed in sec. 2.3.1 is typical of this category, and in all these cases the coefficient of the logarithmic divergence is  $1/3$ . The second type of behavior has a single element in the zero-contact angle case. This case has always infinite slope at  $r_0 = 1$ , but there is a non-zero curvature at the wall for all  $\lambda < \lambda_c$  given by  $r''(z)$ , at the contact point  $(r, z) = (1, H)$ , see fig. 7. The coefficient of the logarithmic divergence for the zero-contact angle case is  $1/\sqrt{3}$ . Perhaps more significantly, this case is mathematically identical to the spinning bubble.

Our results for the spinning bubble have distinctly practical implications for the measurement of surface tension. The analysis of eq. (26) shows that when  $\lambda = 4$  the bubble length diverges – while volume conservation requires that the radius of the straight-cylindrical region decrease. This is why the spinning bubble can only operate arbitrarily close to but not at  $\lambda = 4$ . In practical terms, however, this distinction is unimportant since, when an instrument spins to produce a bubble with, say,  $H = 5$  (i.e. the half length is 5 times the maximum radius), the theory indicates that  $\lambda \approx 4 - 2.8 \times 10^{-3}$ . Hence, for all practical purposes a bubble with  $H = 5$  can be considered to be in critical configuration with  $\lambda = 4$ . Joseph's [2] argument that bubbles with  $H > 2$  can be considered to be at  $\lambda = 4$  is inaccurate, as the present calculation predicts that  $\lambda \approx 3.48$  when  $H = 2$ . A bubble with  $H = 2$  may thus not be long enough to be considered “critical”. As the plot

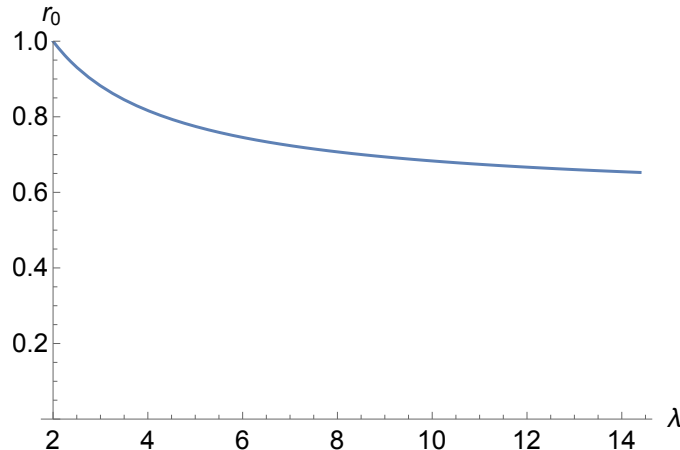


**Figure 14:**  $r_0$  vs.  $\lambda$  between  $\lambda_{\min} = 2$  and  $\lambda_c \approx 14.385$ , for  $\alpha = \pi/3$  (60-deg contact angle).

of fig. 8 shows,  $H = 2$  is close to but not yet in the limiting long- $H$  regime where volume increases linearly with  $H$ . The error in surface tension arising from assuming  $\lambda = 4$  with  $H = 2$  is 13% but drops to 0.07% for  $H = 5$ .

In principle the experimenter need not assume  $\lambda = 4$ , however, since we now have the ratio of bubble half-length to maximum radius,  $H(\lambda)$ , described with a uniformly convergent asymptotic approximant (see Sec. 2.5) over the entire range  $0 \leq \lambda < 4$ . Thus, the approximant for the bubble length allows one to extend surface tension measurement to arbitrary values of  $\lambda$  with just a simple evaluation of  $H_A(\lambda)$  which can be measured by the ratio of bubble half-length to maximum radius. In the absence of gravity, the approximant allows measurements in the intermediate- $\lambda$  region where the sensitivity to error in  $H$  is still moderate. But working at a lower than critical  $\lambda$  has the drawback that it would require precise measurements of both radius *and* length.

## 4 Summary and conclusion

We have reexamined the problem of interface shapes in fluid systems under rigid-body rotation with a focus on finding exact solutions and the asymptotics of singular behaviors near  $\lambda_c$ . We studied two configurations of practical importance, e.g., a meniscus spanning the rotating container radius with arbitrary contact angle at the container wall; and a spinning bubble where the meniscus does not contact the container wall. Finding the asymptotic behavior of the each meniscus configuration length as the critical rotation is approached and the series solution about  $\lambda = 0$  is important not

only because of its intrinsic theoretical interest; it also has application in controlling such interfaces in processes of practical relevance, for example, a rotating reactor or a spinning bubble tensiometer. Knowing the form of the asymptotic divergence, one may construct efficient asymptotic approximants to evaluate each meniscus length at any rotation velocity uniformly and without solving a differential equation numerically.

In conclusion, this work provides analyses that advance the interpretation of interface shapes of fluids in rigid body rotation. The analyses are strictly valid in zero-gravity, but their validity may be extended to normal gravity as long as the gravitational Bond number,  $\rho g R^2 / \sigma$ , is much smaller than  $\lambda$ . For two canonical configurations (meniscus spanning container radius and spinning bubble) we have found exact solutions over the whole range of  $\lambda$  and asymptotic behaviors near critical rotation. To remedy the poor convergence of the infinite-sum exact solutions we constructed convergent asymptotic approximants that greatly improve the convergence efficiency of the exact solution. Our results provide proof of concept of useful analytical calculation tools for applications ranging from controlling rotating reactors to measurement of surface tension with the spinning bubble method.

## Acknowledgement

R. Balasubramaniam helped me formulate initial ideas and calculations and provided a critical sounding board during our frequent discussions. More recently, Steven Weinstein and Nathan Barlow taught me all I know about approximants, suggested the approximant form used here, and guided me through many details of the calculations of the infinite sums presented in the exact solutions. Last but not least, Steven Weinstein's critical reading yielded many suggestions that improved the presentation.

## Appendix A Evaluation of $C_n$ in eq. (40)

In this section we show an evaluation for  $C_n$  that does not require the use of recursions. Because  $f(r, \lambda) \equiv \sin(\theta) \leq 1$ , we attempt expanding the denominator in  $h' = f / \sqrt{1 - f^2}$  as a series in powers of  $f$ . This gives:

$$h' = \frac{f}{\sqrt{1 - f^2}} = \sum_{m=0}^{\infty} f^{2m+1} \frac{\Gamma(\frac{1}{2} + m)}{\sqrt{\pi} \Gamma(m + 1)}. \quad (45)$$

Note that this is just the product of  $f$  by the series of even powers for the denominator. Now expand the powers of  $f = r + \frac{\lambda}{8}(r - r^3)$  using binomial theorem:

$$f^{2m+1} = \sum_{i=0}^{2m+1} \frac{(2m+1)!}{i!(2m+1-i)!} \left(\frac{\lambda}{8}\right)^{2m+1-i} r^i (r - r^3)^{2m+1-i}. \quad (46)$$

A closed-form is available for the integration of the  $r$ -dependence in the above sum:

$$\int_0^1 f^{2m+1} dr = \sum_{i=0}^{2m+1} \frac{(2m+1)!}{i!(2m+1-i)!} \left(\frac{\lambda}{8}\right)^{2m+1-i} \frac{\Gamma(1+m)\Gamma(2m+2-i)}{2\Gamma(3m+3-i)}. \quad (47)$$

We now use this to write the  $r$ -integral of eq. (45) as:

$$\begin{aligned} H(\lambda) &= \sum_{m=0}^{\infty} \frac{\Gamma(\frac{1}{2}+m)\Gamma(2m+2)}{\sqrt{\pi}} \sum_{i=0}^{2m+1} \left(\frac{\lambda}{8}\right)^{2m+1-i} \frac{1}{2\Gamma(i+1)\Gamma(3m+3-i)} \\ &= \sum_{p=0}^{\infty} C_p \lambda^p. \end{aligned} \quad (48)$$

It remains to extract the coefficient of  $\lambda^p$ ,  $C_p$ . Let  $2m+1-i=p$ . To extract the  $p$ -th power from the double sum in eq. (48), for each  $m$  set  $i=2m+1-p$  in the finite  $i$ -index sum. It follows that the coefficient of  $\lambda^p$  is the result of an infinite sum:

$$C_p = \frac{1}{2\sqrt{\pi}} \frac{1}{8^p} \sum_{m=m_0}^{\infty} \frac{\Gamma(\frac{1}{2}+m)\Gamma(2m+2)}{\Gamma(2m+2-p)\Gamma(2+m+p)}. \quad (49)$$

For a given  $p$ , the argument of  $\Gamma(2m+2-p)$  in the denominator cannot be less than 1, i.e.,  $2m+1 \geq p$ . This sets the lowest  $m$  in the sum, as  $m \geq m_0 \geq (p-1)/2$ . When  $p$  is odd, this condition sets the lowest  $m$  directly; when  $p$  is even, the lowest  $m$  is the smallest integer that is larger than  $(p-1)/2$ .

## References

- [1] Bernard Vonnegut. Rotating bubble method for the determination of surface and interfacial tensions. *Rev. Sci. Instrum.*, 13(1):6–9, 1942.
- [2] Howard H. Hu and Daniel D. Joseph. Evolution of a liquid drop in a spinning drop tensiometer. *J. Colloid Interface Sci.*, 162:331–339, 1994.
- [3] James G. Seibold. Configuration and stability of a rotating axisymmetric meniscus at low g. Engineering Degree Thesis, 1965.
- [4] Daniel D. Joseph and Luigi Preziosi. Stability of rigid motions and coating films in bicomponent flows of immiscible liquids. *J. Fluid Mech.*, 185:323–351, 1987.

- [5] D. K. Ross. The shape and energy of a revolving liquid mass held together by surface tension. *Aust. J. Phys.*, 21:823–835, 1968.
- [6] S. Chandrasekhar. The stability of a rotating liquid drop. *Proc. R. Soc. Lon. Ser-A*, 286:1–26, 1965.
- [7] N. S. Barlow, C. R. Stanton, N. Hill, S. J. Weinstein, and A. G. Cio. On the summation of divergent, truncated, and underspecified power series via asymptotic approximants. *The Quarterly Journal of Mechanics and Applied Mathematics*, 70(1):21–48, 01 2017.
- [8] C. D. Manning and L. E. Scriven. On interfacial tension measurement with a spinning drop in gyrostatic equilibrium. *Rev. Sci. Instrum.*, 48:1699–1705, 1977.
- [9] Peter Henrici. Automatic computations with power series. *J. ACM*, 3(1):10–15, January 1956.
- [10] Carl M. Bender and Steven A. Orszag. *Advanced mathematical methods for scientists and engineers*. McGraw-Hill, Inc., 1978.
- [11] Anthony Harkin, Adam Giannarese, Nathaniel S. Barlow, and Steven J. Weinstein. The Rayleigh collapse of two spherical bubbles, 2021, arXiv:2102.05222 [physics.flu-dyn].